

# Southern Ocean summer warming is regulated by storm-driven mixing

Received: 6 August 2024

Accepted: 16 October 2025

Published online: 3 December 2025

 Check for updates

Marcel D. du Plessis<sup>1</sup>✉, Sarah-Anne Nicholson<sup>2</sup>, Isabelle Giddy<sup>1</sup>, Pedro M. S. Monteiro<sup>3</sup>, Channing J. Prend<sup>4</sup> & Sebastiaan Swart<sup>1,5</sup>

The Southern Ocean absorbs most of the excess heat resulting from climate change. However, climate projections show a persistent warm summer bias in its sea surface temperatures, indicating a limited understanding of the air–sea heat exchange mechanisms governing this region. Here we examine the impact of storms on the interannual variability of Southern Ocean surface temperatures during summer using in situ observations from underwater and surface robotic vehicles, climate reanalyses and satellite data. We show that synoptic-scale storms regulate summer sea surface temperatures through alteration of the effective heat capacity of the mixed layer and the entrainment of colder water from below. Storms reduce the summer ocean heat gain by limiting solar radiation reaching the surface. This effect is partially offset by a reduction in heat loss due to turbulent air–sea exchange. We also find that interannual variations in sea surface temperature during summer in the Southern Ocean are driven by changes in storm-mean wind speeds, which are linked to the Southern Annular Mode. Our results demonstrate a causal link between storm forcing and sea surface temperature variability, which is critical for reducing warming biases in climate models and improving future climate projections.

Sea surface temperature (SST) variability in the Southern Ocean influences global climate by driving marine heatwaves<sup>1</sup>, altering annual sea-ice extent<sup>2,3</sup> and setting long-term ocean warming and heat uptake<sup>4,5</sup>. Yet, in this region, climate model projections exhibit a warm bias of up to 2.5 °C during austral summer—equivalent to roughly 100% of the seasonal cycle of SST<sup>6</sup>. This bias has more than doubled from CMIP5 to CMIP6 generation models<sup>7</sup> due to a combination of processes either misrepresented or not resolved in the models. Several mechanisms have been proposed to cause this bias, including the modulation of Ekman flow by the Southern Annular Mode (SAM)<sup>3,8</sup>, misrepresentation of air–sea heat fluxes<sup>7,9</sup> and changes in the strength of the Atlantic meridional overturning circulation<sup>10,11</sup>. However, the role of shorter timescale dynamics, such as synoptic weather (2–6 days), on longer-term SST variability has received little attention due to the difficulty of obtaining

upper-ocean measurements at sufficient temporal (hours) and vertical (metres) resolution across the seasons.

In the Southern Ocean, synoptic-scale air–sea interactions are strongly impacted by mid-latitude cyclones or storms<sup>12,13</sup>. The effect of storms on SST variability at shorter timescales (hours to days) is well studied<sup>14,15</sup>, however, their impact on longer-term changes (months to years) is yet to be understood. For example, storms are expected to intensify and shift poleward under climate change<sup>16,17</sup>, which would influence mid- to high-latitude stratification dynamics and SST at interannual and decadal timescales<sup>18</sup>. These changes, in turn, will have far-reaching consequences for the oceanic CO<sub>2</sub> reservoir, mixed-layer nutrient supply and the global energy budget<sup>19–22</sup>.

This study examines the impact of storms on the synoptic to interannual variability of Southern Ocean SST during the austral summer

<sup>1</sup>Department of Marine Sciences, University of Gothenburg, Gothenburg, Sweden. <sup>2</sup>Southern Ocean Carbon-Climate Observatory, CSIR, Cape Town, South Africa. <sup>3</sup>School for Climate Studies, Stellenbosch University, Stellenbosch, South Africa. <sup>4</sup>School of GeoSciences, University of Edinburgh, Edinburgh, UK. <sup>5</sup>Department of Oceanography, University of Cape Town, Rondebosch, South Africa. ✉e-mail: [marcel.du.plessis@gu.se](mailto:marcel.du.plessis@gu.se)

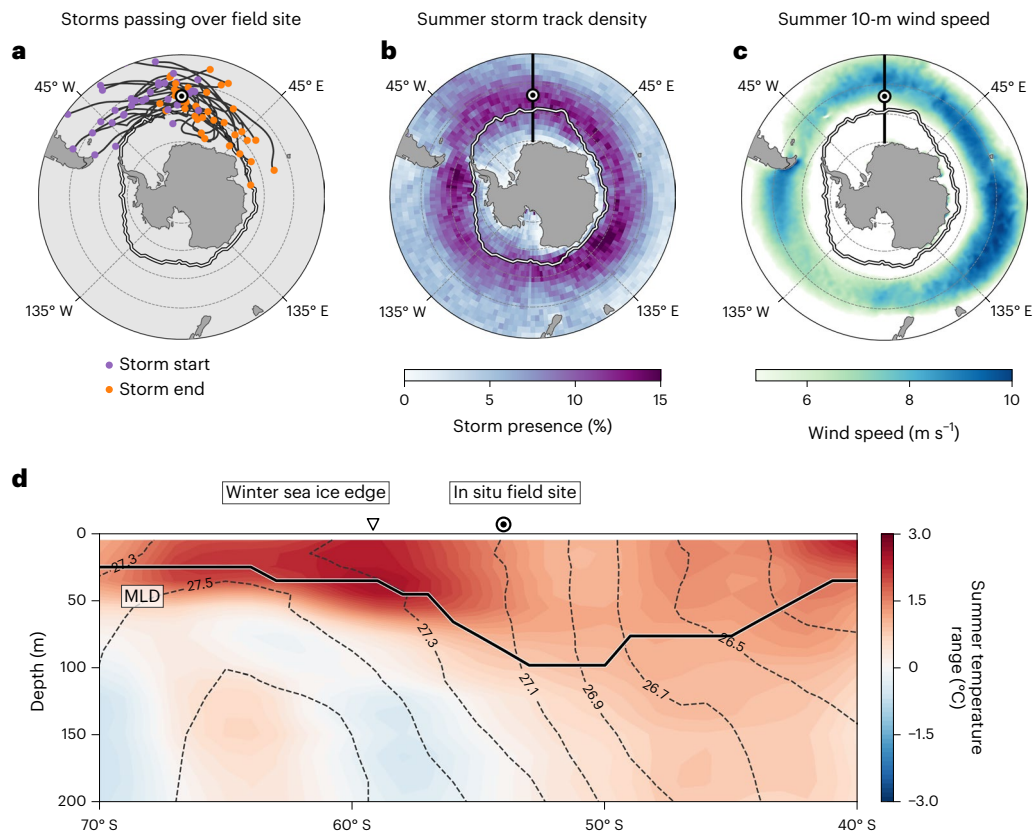


**Fig. 1 | Summer storm activity and temperature change at the SOSCEX-Storm Southern Ocean field site.** **a**, Individual storms tracks passing within 1,000 km of the SOSCEX-Storm field site (black and white dot at 54° S, 0° E). Storm tracks obtained from ref. 27. White line is the December-mean sea-ice edge for 2018 from the NOAA Optimum Interpolation SST V2 product<sup>55</sup>. **b**, Summer (December to February) climatology of storm track density from 1981 to 2019, showing presence in percentage terms on a 1° × 1° grid. **c**, Summer-mean 10-m

wind speed ( $\text{m s}^{-1}$ ) for the duration of the SOSCEX-Storm field campaign. **d**, Black solid line indicates the location of the upper-ocean temperature range ( $^{\circ}\text{C}$ ) along 0° E from February 2019 and December 2018 using a collection of ocean temperature profiles obtained across the global oceans (EN4; see Methods). Overlaid dashed grey contours represent potential density anomalies ( $\sigma_{\theta}$ ,  $\text{kg m}^{-3}$ ). The thick black line indicates the MLD. Basemaps in **a–c** from Natural Earth (<https://www.naturalearthdata.com>).

period (December to February), when model SST biases are largest<sup>6</sup>. Using in situ observational evidence from ocean robotics, we show that storm-driven mixing sets the summer evolution of SST in the subpolar Southern Ocean. We upscale these local observations to the ice-free Southern Ocean from 1981 and 2019 to show that interannual changes in the summertime SST are directly related to wind speed inside storms, which are driven by the SAM. In other words, we show that the modulation of SST by climate-scale variability is exerted through the synoptic processes that set the seasonal warming.

### Seasonal ocean warming rate regulated by storms

During the austral summer of 2018–2019, a 79-day field campaign, ‘SOSCEX-Storm,’ was conducted to study storm impacts on upper-ocean variability. In situ observations were collected from an autonomous underwater Slocum glider and a surface Wave Glider in the subpolar region (Fig. 1 and Extended Data Fig. 1). Here frequent and intense storms (Fig. 1a–c) contribute to the deeper summer-mean mixed-layer depths (MLDs) than those to the north and south (Fig. 1d). The greater heat capacity of these deeper MLDs suppresses summer SST warming ( $-1^{\circ}\text{C}$ ) compared to adjacent regions ( $-3^{\circ}\text{C}$ ).

Glider measurements show the SST increasing from 0.6  $^{\circ}\text{C}$  at deployment to a summer maximum ( $T_{\text{max}}$ ) of 2.28  $^{\circ}\text{C}$  about 2 months later (Fig. 2a). This warming was predominantly driven by positive shortwave radiation (Fig. 2f; note positive heat fluxes represent ocean heat gain), with daytime peaks between 219  $\text{W m}^{-2}$  and 921  $\text{W m}^{-2}$ . Intermittent periods of positive turbulent heat fluxes—a combination of sensible and latent heat flux—exceeded 40  $\text{W m}^{-2}$  on average every

5.4  $\pm$  3.3 days, probably associated with the passage of storms. Yet, on average across the entire field campaign, the latent heat flux was negative ( $-13.6 \text{ W m}^{-2}$ ), reflecting ocean heat loss through evaporation. Meanwhile, sensible heat fluxes averaged 7.5  $\text{W m}^{-2}$  but reached up to 116  $\text{W m}^{-2}$  (Fig. 2d). Thus, the seasonal warming of SST was due primarily to solar radiation, with sensible heat flux acting as a secondary source of ocean warming. This warming was partially offset by the evaporative latent heat flux, longwave radiation and the entrainment of colder waters into the mixed layer from below, which we demonstrate using a simplified model of the mixed-layer temperature considering only the air–sea heat flux and entrainment terms (Methods, Fig. 2a and Extended Data Fig. 2). The observed and modelled SST are remarkably consistent ( $r^2 = 0.98$ ,  $P < 0.001$ ,  $n = 79$ ), despite a model warm bias of 0.13  $^{\circ}\text{C}$  (Fig. 2a). This warm bias may be due to excess downwelling shortwave radiation in the ERA5 reanalysis model<sup>23,24</sup>, or unresolved advective processes. However, the high correlation between observed and modelled SST demonstrates that the summer warming was governed by the balance between air–sea heat fluxes and entrainment.

The warming rate, which helps set  $T_{\text{max}}$ , is largely controlled by changes in the mixed-layer effective heat capacity, which is driven by variations in MLD. To demonstrate this, the observed summer evolution of SST can be separated into four periods of relatively consistent warming rates (horizontal lines in Fig. 2a). In the first warming period (days –12 to 5), deep MLDs and a mean net heat flux of 179  $\text{W m}^{-2}$  across the 17 days resulted in an average SST warming rate of 0.012  $^{\circ}\text{C d}^{-1}$ . This increased by 325% to an average of 0.051  $^{\circ}\text{C d}^{-1}$  between days 5 to 23 (second period), despite no change in the mean net heat flux (180  $\text{W m}^{-2}$ ).

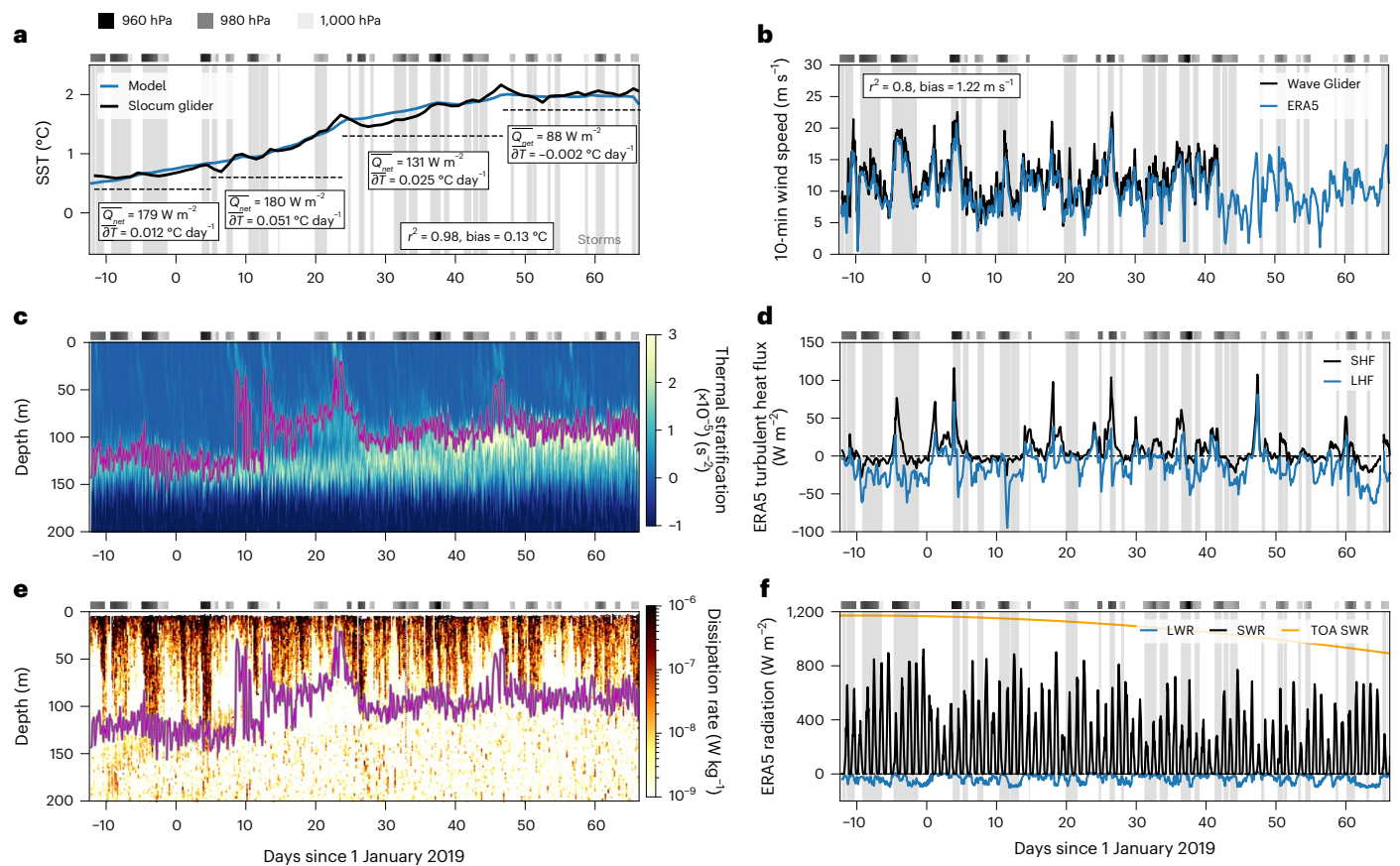


**Fig. 2 | Summer warming regulated by storm-driven mixed-layer depth variability.** **a**, Time series of summer SST from the underwater glider (black line) and model (blue line). Grey markers above indicate storm presence with associated minimum sea-level pressure (in hPa). **b**, Wind speed measured from the surface Wave Glider (adjusted to 10 m above sea level, black line) and 10-m wind speed from the ERA5 reanalysis (blue line). **c**, Thermal-component of the Brunt–Väisälä frequency ( $s^{-2}$ ) measured from the glider, with the MLD in purple.

**d**, ERA5 turbulent heat fluxes: sensible heat flux (SHF, black line) and latent heat flux (LHF, blue line) in  $W m^{-2}$ , with positive values denoting ocean heat gain. **e**, Dissipation rate ( $W kg^{-1}$ ) from the glider plotted here as a measure of turbulent mixing intensity, with MLD in purple. **f**, ERA5 radiative fluxes: longwave radiation (LWR, blue line), shortwave radiation (SWR, black line) and the top-of-atmosphere incoming shortwave radiation (TOA SWR, orange line) in units of  $W m^{-2}$ . Grey shaded regions in all panels indicate storm periods.

The lower SST warming rate during the first period coincided with a series of intense (central pressure below 970 hPa) storms identified using a Lagrangian storm tracking method (Methods). Associated enhanced wind speeds, exceeding  $15 m s^{-1}$  (Fig. 2b), led to high levels of turbulent ocean mixing below the MLD (Fig. 2e) that kept stratification low (Fig. 2c) and the mixed-layer deep ( $123 \pm 11 m$ ). Between days 5 and 11 (onset of second period), a series of weaker storms (central pressure above 980 hPa) with wind speeds below  $10 m s^{-1}$  allowed the strongly positive net heat flux to restratify the surface ocean (Fig. 2c). The mixed layer shoaled rapidly—by between 67 and 113 m in a day—on days 8, 12 and 22, remaining relatively shallow (about 70 m) between these events. During this time (18% of the summer season), the SST increased by  $0.96 ^\circ C$ , accounting for 61% of the entire summer SST increase.

During the third period (days 23 to 47), a series of intense storms deepened the mixed layer to about 100 m. This, along with a reduction of the mean net heat flux to  $131 W m^{-2}$ , decreased the SST warming rate to  $0.025 ^\circ C d^{-1}$ . The drop in heat flux was primarily due to the reduction in incoming top-of-atmosphere shortwave radiation (Fig. 2f). That said, with the positive net heat flux still large, the SST continued to increase until reaching the seasonal maximum ( $T_{max} = 2.28 ^\circ C$ ). After this, the SST remained comparatively stable at  $-0.002 ^\circ C d^{-1}$  as the net heat flux reduced to  $88 W m^{-2}$ , again due to a drop in incoming shortwave radiation (Fig. 2f). This slightly negative SST tendency—despite the positive heat flux—can be explained by a multi-day entrainment-driven cooling associated with deep turbulent mixing, starting on day 47 (Fig. 2e and Extended Data Fig. 3). Thus, in addition to regulating MLD and the

mixed-layer's heat capacity, intense storms can reduce SST through wind-driven entrainment of cooler subsurface water. This is seen during two other notable SST cooling events in response to mixing below the MLD, on days 5 and 24 (Fig. 2a,c). Cumulatively, all three entrainment events reduced the SST by about  $1 ^\circ C$  over the summer (Fig. 2a), with the two strongest events cooling the SST by  $0.4 ^\circ C$  each (days 24 to 27 and days 47 to 52). These large SST changes, caused by individual storms, highlight the rectified effect of storm-driven entrainment on the seasonal-scale warming during summer.

### Storm controls on the air–sea heat flux

The passage of storms over the field site was associated with synoptic bursts of positive turbulent heat fluxes lasting several days (Fig. 2d), which were often preceded by reduced shortwave radiation and increased longwave radiation (Fig. 2f). These patterns are characteristic of warm, moist air from lower latitudes being advected over a cooler ocean<sup>14</sup> and an increase in cloudiness forming along the warm front<sup>24</sup>. Indeed, on average for all storms during the field campaign, elevated turbulent fluxes coincided with northwesterly winds (Fig. 3b) transporting subtropical air polewards. Meanwhile, the reduced shortwave radiation (Fig. 3e) and increased longwave radiation (Fig. 3f) were, on average, linked to northeasterly winds in the leading edge of the storm (Fig. 3b). Here thick stratiform clouds form a cloud shield<sup>25</sup> with high albedo that reflects downwelling shortwave radiation<sup>26</sup>. Thus, storm-driven air–sea heat flux depends on the sector of the storm considered (Extended Data Fig. 4).

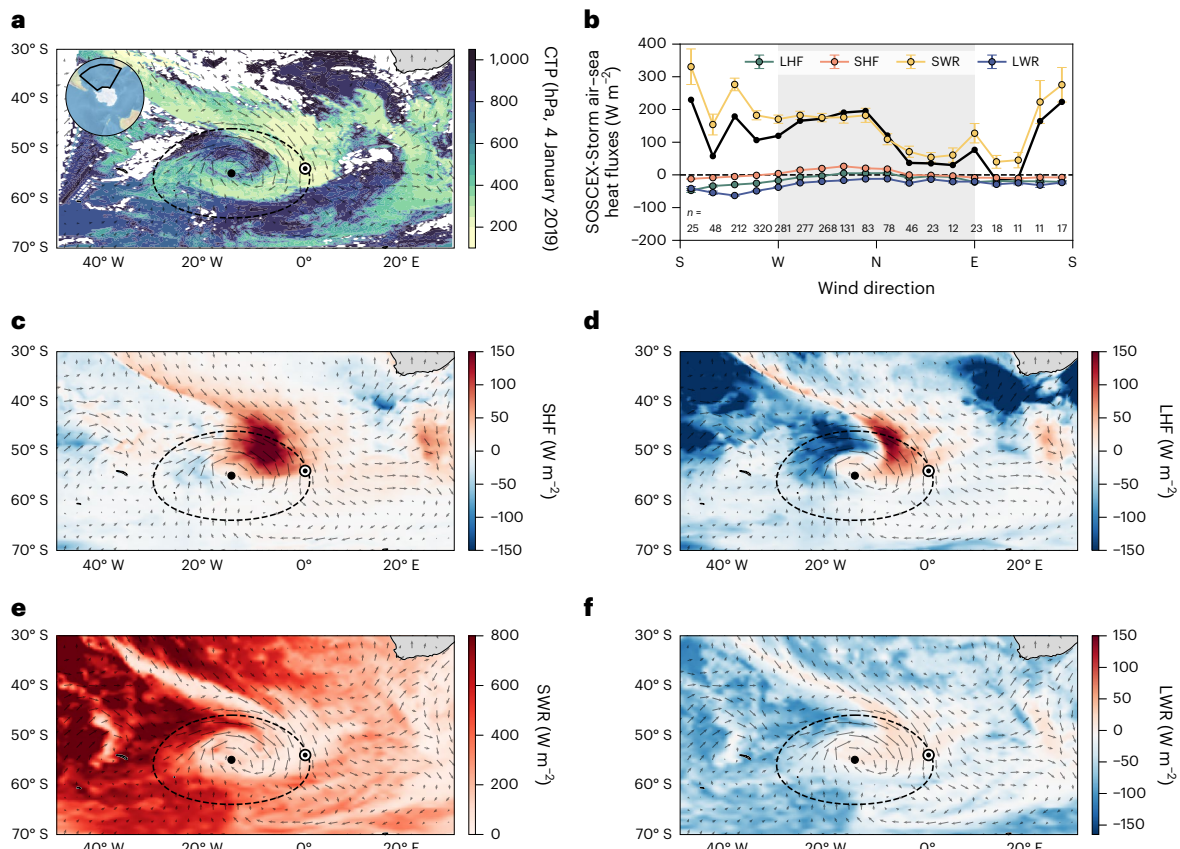


**Fig. 3 | Storm impacts on air-sea flux variability during SOSCEX-Storm.**

**a**, Cloud top pressure (CTP, in hPa) on 4 January 2019 from the Moderate Resolution Imaging Spectroradiometer (MODIS) satellite L2 data, showing the spatial extent of a large storm. Map inset shows region of the maps. **b**, Air-sea heat fluxes binned by wind direction. Dots show the mean LHF (green), SHF (orange), SWR (gold) and LWR (blue), with error bars indicating standard error of the mean.  $n$  values for each wind direction bin placed along the bottom of the panel. The black line is the net heat flux. The shaded region denotes northerly winds. **c-f**, Snapshot

of the ERA5 heat flux components depicting a storm passing over the in situ robotic platforms on the same day as the CTP observations at 17:00 UTC. ERA5 reanalysis data for SHF (**c**), LHF (**d**), SWR (**e**) and LWR (**f**). Black arrows in **a, c-f** represent the ERA5 10-m wind vectors, with the black dot showing the storm centre and the black dashed ellipse a 1,000-km radius around the storm centre. The black and white dots show the location of the SOSCEX-Storm field campaign. Positive heat fluxes denote ocean heat gain. Basemaps in **a** and **c-f** from Natural Earth (<https://www.naturalearthdata.com>).

Next, we examined the air-sea flux structure within all summer storms across the ice-free Southern Ocean from 1981 to 2019, identified with a Lagrangian tracking algorithm that uses ERA5 mean sea-level pressure<sup>27</sup> (Fig. 4a-d). The mean storm structure is consistent with the findings from the SOSCEX-Storm experiment (Fig. 2d,f and Extended Data Fig. 4). Both show a reduction of shortwave radiation along the warm front region, albeit still largely positive at around  $100 \text{ W m}^{-2}$  (Fig. 4c). In addition, the warm sector shows the weakest net longwave and evaporative cooling (both around  $-20 \text{ W m}^{-2}$ ) and the strongest sensible heating ( $20 \text{ W m}^{-2}$ ) (Fig. 4a,b,d). Conversely, in the cold sector, the strongest ocean heat loss for all of longwave radiation, latent heat flux and sensible heat flux was found at  $-50 \text{ W m}^{-2}$ ,  $-60 \text{ W m}^{-2}$  and  $-15 \text{ W m}^{-2}$ , respectively. Nevertheless, under the reduced cloudiness, shortwave radiation was  $300 \text{ W m}^{-2}$  (Fig. 4c), resulting in net ocean heat gain.

The mean air-sea fluxes within these summer storms exhibit distinct regionality within the Southern Ocean (Fig. 4e-h). At subpolar latitudes, storms drive a mean ocean heat loss of about  $-15 \text{ W m}^{-2}$ , due to the latent heat flux. Meanwhile, large swaths of the Atlantic and Indian sectors and parts of the western Pacific show ocean heat gain of about  $10 \text{ W m}^{-2}$  due to the sensible heat flux (Fig. 4e,f). In general, both turbulent fluxes are between 20 and  $40 \text{ W m}^{-2}$  greater than in more northern regions of the Southern Ocean, which can be attributed to the poleward transport of warm, moist air originating from subtropical latitudes; notably, 74% of summer storms move poleward from their

genesis point (Extended Data Fig. 5). Indeed, summertime storms drive consistently less negative (or more positive) latent and sensible fluxes (Fig. 4i). Similarly, storms reduce ocean heat loss by LWR, presumably by increasing the downwelling component due to increased cloud cover. This combined effect of reduced ocean heat loss (or heat gain) is outweighed by the substantial reduction in shortwave radiation due to storm-related cloud cover. Consequently, storms reduce the total heat uptake by the Southern Ocean, highlighting their key role in atmosphere-ocean heat exchange.

### Storm-driven impacts on summer SST across the Southern Ocean

To assess the role of storms in Southern Ocean summer SST variability, we first correlate interannual changes in summer-mean net air-sea heat flux with summer  $T_{\text{max}}$ , which is highly coherent with the summer-mean SST ( $r = 0.95$ ,  $P < 0.001$ ,  $n = 39$ ; Extended Data Fig. 6) and a key metric for marine heatwaves<sup>28</sup> and ocean stratification<sup>18</sup>. The air-sea heat flux and summer  $T_{\text{max}}$  correlation is mostly non-significant across the Southern Ocean ( $P > 0.1$ ); however, statistically significant positive correlations are found in the eastern Pacific and parts of the northern Indian sector (Fig. 5a). In these regions, air-sea heat fluxes drive interannual variations in summer SST. Conversely, some areas of the significant negative correlation occur in the Indian sector of the subpolar Southern Ocean, where  $T_{\text{max}}$  is cooling in response to a more positive flux. This counter-intuitive response demonstrates that other factors, such as

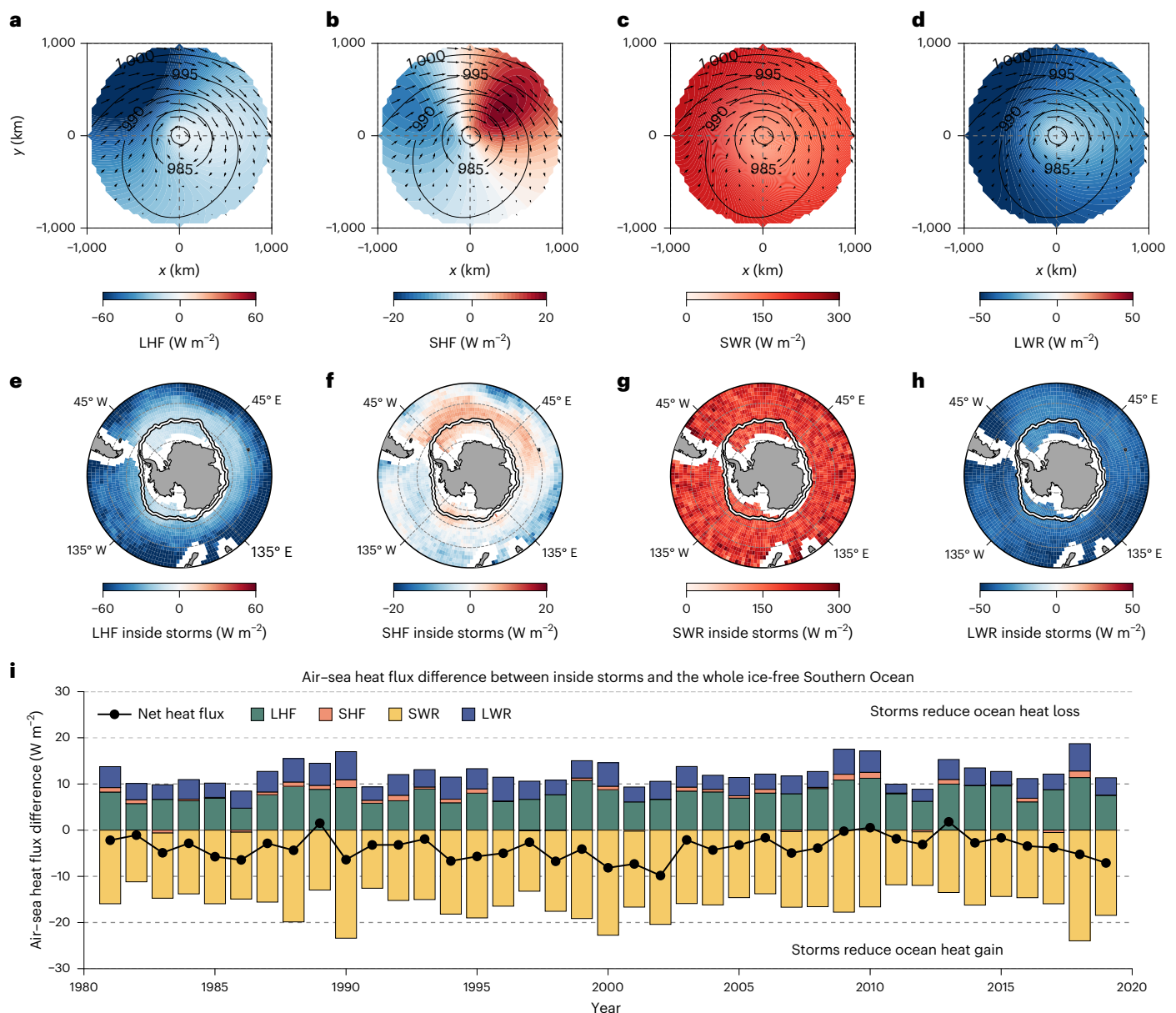


**Fig. 4 | Summer storm-composited heat fluxes across the Southern Ocean.** **a–d**, Storm composite mean of LHF (**a**), SHF (**b**), SWR (**c**) and LWR (**d**) during all summer months between 1981 and 2019 based on ERA5 reanalysis. Overlaid black contours show the mean sea-level pressure (MSLP) in hPa, and black arrows indicate 10-m wind vectors. **e–h**, Summer-mean air-sea heat flux within storms between 1981 and 2019 for LHF (**e**), SHF (**f**), SWR (**g**) and LWR (**h**). **i**, Stacked bars

show the difference of the summer-mean air-sea heat flux components (LHF (green), SHF (orange), SWR (gold), LWR (blue)) from within storms only and the whole ice-free Southern Ocean average. Units are in  $\text{W m}^{-2}$ . The black dashed line with markers indicates the net heat flux difference, representing the sum of all components. Basemaps in **e–h** from Natural Earth (<https://www.naturalearthdata.com>).

MLD deepening and entrainment, or increased upwelling in response to stronger westerlies<sup>29</sup>, set the summer  $T_{\max}$ . In other words, while air-sea heat fluxes are critical for determining the overall heat input to the ocean during summer, interannual changes in summer  $T_{\max}$  do not necessarily reflect this heat input.

Meanwhile, there is a significant inverse relationship ( $P < 0.1$ ) across the majority of the Southern Ocean between summer  $T_{\max}$  and the summer-mean wind speed (Fig. 5b), which we use as a proxy for storm-driven winds due to their strong coherence ( $r = 0.77$ ,  $P < 0.001$ ; Extended Data Fig. 7). Namely, years with higher summer-mean wind speeds consistently correspond to lower  $T_{\max}$ . This coherence has previously been attributed to Ekman transport<sup>30</sup>. Integrating the daily-mean temperature tendency due solely to Ekman transport for each summer from 1981 and 2019 (Extended Data Fig. 8), shows substantial cooling,

averaging about  $0.6\text{ }^{\circ}\text{C}$  across the Southern Ocean and exceeding  $4\text{ }^{\circ}\text{C}$  in regions with strong SST gradients, such as western boundary currents and Antarctic Circumpolar Current fronts (not shown), consistent with previous research<sup>3,31</sup>. However, the interannual variability of this Ekman-driven cooling is small, accounting for only about 10% of the summer  $T_{\max}$  anomalies across the Southern Ocean.

Because Ekman transport explains only a small fraction of the interannual temperature change, the correlation between  $T_{\max}$  and winds must arise from other processes. We consider the strong positive correlation between summer-mean wind speed and summer-mean MLD across the Southern Ocean (Fig. 5c)—possible given the good coverage of summer MLD values across the Southern Ocean (Extended Data Fig. 9). These deeper mixed layers, in turn, consistently correlate with lower  $T_{\max}$  values (Fig. 5d), which could result from an

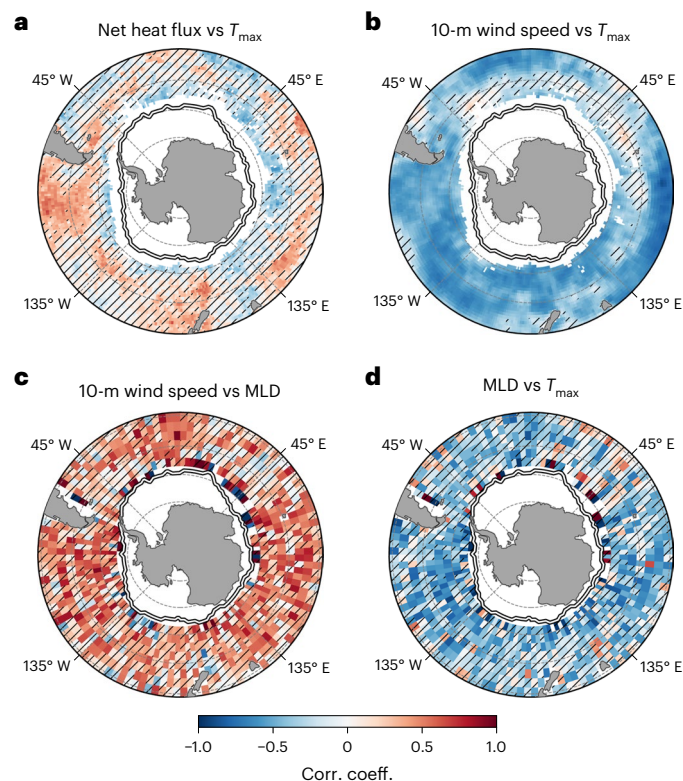


**Fig. 5 | Interannual co-variability between the summer wind speed, MLD and  $T_{\max}$ .** **a–d**, Spatial correlation maps showing the interannual relationships (2004–2019) of the summer-mean: net heat flux and maximum SST ( $T_{\max}$ ) (**a**); 10-m wind speed and  $T_{\max}$  (**b**); 10-m wind speed and MLD (**c**) and MLD and  $T_{\max}$  (**d**). Shading indicates the correlation coefficient (Corr. coeff.), whereas stippling denotes areas where the correlation is not statistically significant at the 90% confidence level ( $P > 0.1$ ,  $n = 16$ ). Basemaps from Natural Earth (<https://www.naturalearthdata.com>).

increase in the mixed layer's heat capacity or entrainment. Crucially, the strong coherence between the detrended summer-mean wind speed inside storms and across the entire ice-free Southern Ocean (Extended Data Fig. 7) implies that storms are key regulators of Southern Ocean wind-speed intensity, corroborating previous findings<sup>14</sup>.

Whereas there is widespread coherence in the correlations of Fig. 5c,d, only 30% are statistically significant across the ice-free Southern Ocean. We correlate the wind-speed inside storms and  $T_{\max}$  averaged across the Southern Ocean between 2004 and 2019, which supports the widespread spatial patterns observed in Fig. 5b–d, that summers with higher storm wind speeds (anomalies of  $>0.2 \text{ m s}^{-1}$ ) correspond to colder  $T_{\max}$  by up to  $-0.2 \text{ °C}$  (Fig. 6a,  $r = -0.62$ ,  $P < 0.011$ ,  $n = 16$ ). The strong correlation but modest significance probably reflects averaging across regions with opposing signals; eddy-rich areas, for example, exhibit anti-correlations.

To assess the influence of MLD variability on summer  $T_{\max}$ , we evaluated the SST tendency equation,  $Q / (\rho C_p h_m)$ , where  $Q$  is the air–sea heat flux,  $\rho$  is the mixed-layer density,  $C_p$  is the specific heat capacity of seawater and  $h_m$  is the mixed-layer depth. Using the summer-mean air–sea heat flux and MLDs, we compared the simulated interannual SST evolution with a case assuming a fixed, climatological MLD. The resulting temperature difference closely tracks observed variations in the  $T_{\max}$  ( $r = 0.71$ ,  $P < 0.002$ ,  $n = 16$ , root mean square error =  $0.096 \text{ °C}$ ; Fig. 6b), demonstrating that year-to-year changes in MLD alone can drive the observed  $T_{\max}$  anomalies. This highlights MLD variability as a key control on Southern Ocean summer warming, which in turn are linked to storm-driven wind speeds ( $r = 0.43$ ,  $P < 0.09$ ,  $n = 16$ ).

The interannual variations in the storm-mean wind speed are closely tied to the SAM (Fig. 6c,  $r = 0.48$ ), with a positive SAM

accompanying a poleward shift of storm tracks and associated surface westerlies<sup>32</sup>. This suggests that the causal link between climate modes and  $T_{\max}$  variability is exerted via changes in storm activity and associated strong wind speeds.

## Implications

We have shown that summer SST warming rates in the Southern Ocean are linked to storms and the associated turbulent mixing, which controls the MLD, sets its effective heat capacity and drives entrainment of cooler waters from below. Meanwhile, storms also reduce the net heat flux by reducing shortwave radiation, although this is partially offset by elevated turbulent fluxes as storms transport warm air poleward, predominantly in the Atlantic and Indian sectors. Meanwhile, in the Pacific, enhanced ocean heat loss from storms probably stems from the larger air–sea temperature and humidity differences there<sup>33</sup>. This inter-basin asymmetry in the storm impact on turbulent air–sea fluxes may result from intensified storm activity in the Atlantic and Indian sectors, where the subpolar jet stream core coincides with strong SST gradients<sup>13,34</sup>. There, sharp SST gradients align with enhanced storm activity, which in turn modifies the SST gradient through storm-driven turbulent mixing and lateral atmospheric heat exchange<sup>35,36</sup>. This feedback is thought to influence longer-term variability associated with the SAM, whereby positive SAM phases strengthen latitudinal sensible heat flux gradients that maintain the baroclinicity required for recurrent storm development<sup>37</sup>.

Nevertheless, summer SST warming is primarily regulated by storm-driven wind-speed variability that alters MLD—modulated by changes in the SAM. These results corroborate Earth System Model analyses<sup>3</sup> that attribute the spread in Southern Ocean summer warming rates to interannual variations in seasonal MLD shoaling. Because zonally asymmetric MLD anomalies have previously been linked to the SAM<sup>38</sup>, our results point to enhanced storm-driven wind speeds as a key causal mechanism. Indeed, storm-related wind perturbations are estimated to increase the mean Southern Ocean wind stress by nearly 40% (ref. 39), with a corresponding SST response<sup>40</sup>. This also has implications for the ventilation of heat into the ocean interior<sup>41</sup>, sea-ice formation in the subsequent winter<sup>3,42</sup> and the supply of carbon and nutrient-rich deep waters to the surface ocean<sup>43,44</sup>. Future work should investigate these consequences and the interaction between storm-driven mixing and mesoscale variability<sup>45–47</sup>.

Our results help explain the warm SST biases and overly shallow MLDs in models from the 6th Coupled Model Intercomparison Project<sup>6</sup>, which typically underestimate storm frequency and intensity<sup>48</sup>. Overly shallow mixed layers reduce entrainment and the mixed-layer heat capacity, making SSTs more sensitive to surface heat fluxes. Therefore, accurately representing storm–ocean interactions is essential to reduce SST biases in the next generation of climate models. The issue with simulated MLDs is further compounded by an equatorward bias in storm track position<sup>48</sup> and by the misrepresentation of mid-level clouds in Southern Ocean storms<sup>49</sup>—a factor proposed to explain Southern Ocean summer SST biases<sup>79</sup>—which, as our study shows, play a key role in storm-driven reductions of surface radiative warming. It should be noted that these results pertain to summer. In winter, when the air–sea heat flux is negative and the climatological MLDs are deep, mixing is dominated by convection and thus storm-driven wind effects may be less important for SST changes<sup>50,51</sup>. However, the processes controlling summer  $T_{\max}$  may still influence winter SSTs by setting the seasonal stratification at the mixed-layer base. In other words, for summers with stronger stratification, there may be a delayed onset of MLD deepening due to convective cooling.

The relationship between storm activity and the SAM has implications for SST under climate change. The SAM has shown a positive trend in summer due to stratospheric ozone loss<sup>52,53</sup>, with associated stronger and poleward shifted westerlies and an increased occurrence of storms<sup>54</sup>. As winds strengthen, an associated deepening of the MLD<sup>18</sup>

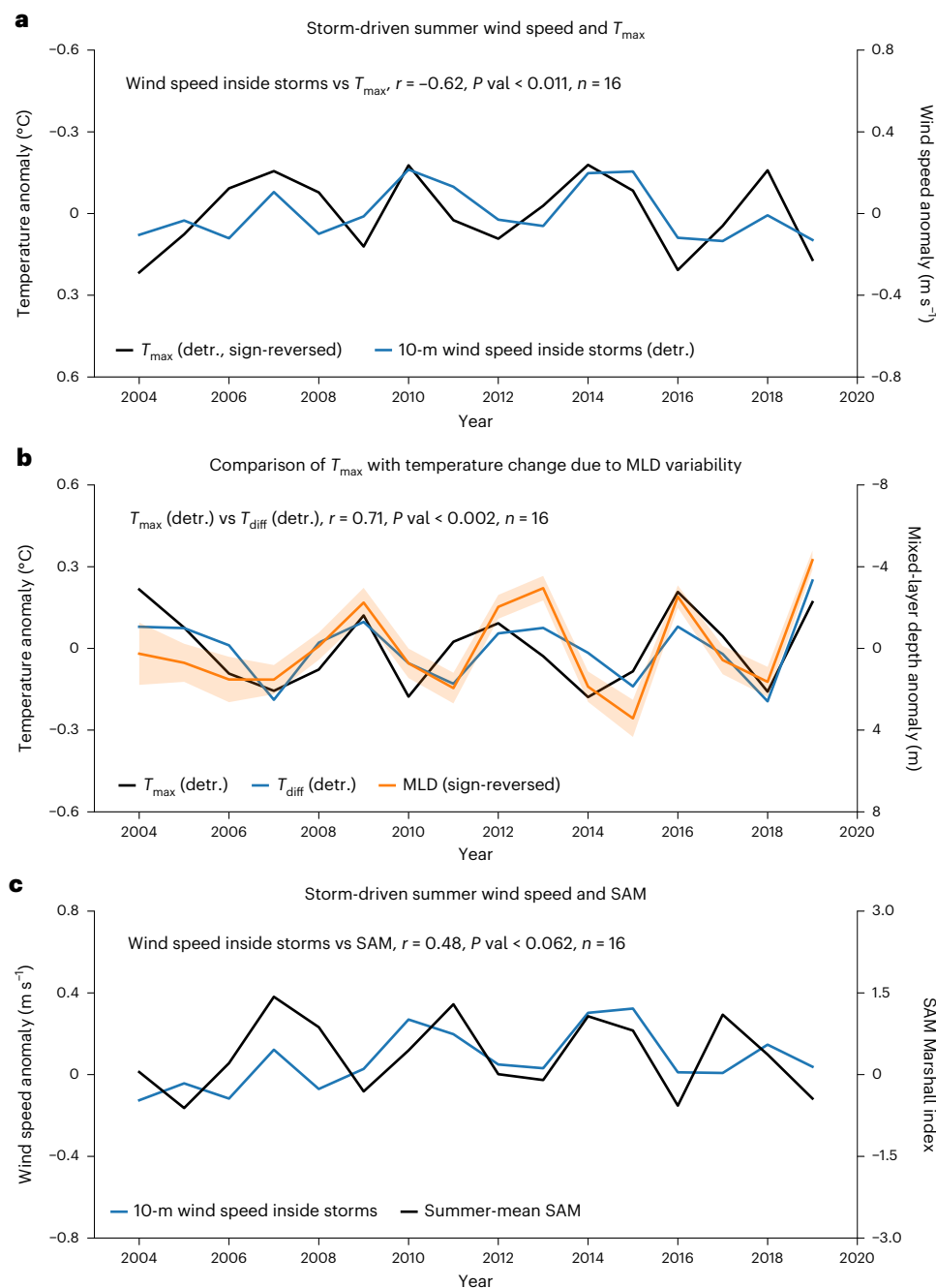


**Fig. 6 | Interannual co-variability between Southern Ocean storm characteristics and SAM. a**, Detrended interannual summertime anomalies of the 10-m mean wind speed inside storms (blue line) and the detrended maximum summer SST (sign-reversed anomaly,  $T_{\max}$ , black line) across the ice-free Southern Ocean (south of  $40^{\circ}\text{S}$ ) over 2004–2019, showing a strong correlation ( $r = -0.62$ ,  $P < 0.011$ ,  $n = 16$ ). **b**, Comparison between detrended  $T_{\max}$  (black line) and the temperature change associated with mixed-layer depth variability ( $T_{\text{diff}}$ ; blue

line), together with the detrended mixed-layer depth anomaly (orange, sign-reversed shading shows  $\pm 1$  standard error of the mean), indicating that shallower summer mixed layers coincide with enhanced surface warming ( $r = 0.71$ ,  $P < 0.002$ ,  $n = 16$ ). The term detr. in **a** and **b** refers to the detrended signal for each respective variable. **c**, Comparison of storm-driven summer 10-m wind-speed anomalies and the SAM Marshall Index, illustrating co-variability between storm wind-speed intensity and the hemispheric circulation ( $r = 0.48$ ,  $P < 0.062$ ,  $n = 16$ ).

could slow future summer SST warming by increasing the mixed-layer effective heat capacity and entrainment. Yet, the Southern Ocean has also increased in stratification<sup>18</sup>, which may slow the subduction of warm surface water to intermediate depths<sup>29</sup>. Constraining these feedbacks requires sustained high-resolution observations that resolve disparate scales of variability. Here we have demonstrated from robotic observations that storms exert key control over the summer evolution of SST and that the influence of storms extend to interannual SST variations during summer. Better understanding of these multi-scale

interactions is necessary to model air–sea exchange processes and predict future changes to the climate system.

### Online content

Any methods, additional references, Nature Portfolio reporting summaries, source data, extended data, supplementary information, acknowledgements, peer review information; details of author contributions and competing interests; and statements of data and code availability are available at <https://doi.org/10.1038/s41561-025-01857-3>.

## References

- Holbrook, N. J. et al. A global assessment of marine heatwaves and their drivers. *Nat. Commun.* **10**, 2624 (2019).
- Meehl, G. A. et al. Sustained ocean changes contributed to sudden Antarctic sea ice retreat in late 2016. *Nat. Commun.* **10**, 14 (2019).
- Wilson, E. A., Bonan, D. B., Thompson, A. F., Armstrong, N. & Riser, S. C. Mechanisms for abrupt summertime circumpolar surface warming in the Southern Ocean. *J. Clim.* **36**, 7025–7039 (2023).
- Swart, N. C., Gille, S. T., Fyfe, J. C. & Gillett, N. P. Recent Southern Ocean warming and freshening driven by greenhouse gas emissions and ozone depletion. *Nat. Geosci.* **11**, 836–841 (2018).
- Hobbs, W. R., Roach, C., Roy, T., Sallée, J.-B. & Bindoff, N. Anthropogenic temperature and salinity changes in the Southern Ocean. *J. Clim.* **34**, 215–228 (2021).
- Wang, Y., Heywood, K. J., Stevens, D. P. & Damerell, G. M. Seasonal extrema of sea surface temperature in CMIP6 models. *Ocean Sci.* **18**, 839–855 (2022).
- Zhang, Q., Liu, B., Li, S. & Zhou, T. Understanding models' global sea surface temperature bias in mean state: from CMIP5 to CMIP6. *Geophys. Res. Lett.* **50**, e2022GL100888 (2023).
- Kostov, Y. et al. Fast and slow responses of Southern Ocean sea surface temperature to SAM in coupled climate models. *Clim. Dyn.* **48**, 1595–1609 (2017).
- Hyder, P. et al. Critical Southern Ocean climate model biases traced to atmospheric model cloud errors. *Nat. Commun.* **9**, 3625 (2018).
- Wang, C., Zhang, L., Lee, S.-K., Wu, L. & Mechoso, C. R. A global perspective on CMIP5 climate model biases. *Nat. Clim. Change* **4**, 201–205 (2014).
- Luo, F., Ying, J., Liu, T. & Chen, D. Origins of Southern Ocean warm sea surface temperature bias in CMIP6 models. *npj Clim. Atmos. Sci.* **6**, 127 (2023).
- Trenberth, K. E. Storm tracks in the Southern Hemisphere. *J. Atmos. Sci.* **48**, 2159–2178 (1991).
- Nakamura, H. & Shimpo, A. Seasonal variations in the Southern Hemisphere storm tracks and jet streams as revealed in a reanalysis dataset. *J. Clim.* **17**, 1828–1844 (2004).
- Yuan, X., Patoux, J. & Li, C. Satellite-based midlatitude cyclone statistics over the Southern Ocean: 2. tracks and surface fluxes. *J. Geophys. Res.: Atmos.* **114**, 2008JD010874 (2009).
- Nonaka, M. et al. Air–sea heat exchanges characteristic of a prominent midlatitude oceanic front in the South Indian Ocean as simulated in a high-resolution coupled GCM. *J. Clim.* **22**, 6515–6535 (2009).
- Dai, P. & Nie, J. Robust expansion of extreme midlatitude storms under global warming. *Geophys. Res. Lett.* **49**, e2022GL099007 (2022).
- Gentile, E. S., Zhao, M. & Hodges, K. Poleward intensification of midlatitude extreme winds under warmer climate. *npj Clim. Atmos. Sci.* **6**, 219 (2023).
- Sallée, J.-B. et al. Summertime increases in upper-ocean stratification and mixed-layer depth. *Nature* **591**, 592–598 (2021).
- Bengtsson, L., Hodges, K. I., Koumoutsaris, S., Zahn, M. & Berrisford, P. The changing energy balance of the polar regions in a warmer climate. *J. Clim.* **26**, 3112–3129 (2013).
- Tamarin-Brodsky, T. Enhanced poleward propagation of storms under climate change. *Nat. Geosci.* **10**, 908–913 (2017).
- Yettella, V. & Kay, J. E. How will precipitation change in extratropical cyclones as the planet warms? Insights from a large initial condition climate model ensemble. *Clim. Dyn.* **49**, 1765–1781 (2017).
- IPCC *The Ocean and Cryosphere in a Changing Climate: Special Report of the Intergovernmental Panel on Climate Change* (Cambridge Univ. Press, 2022).
- McFarquhar, G. M. et al. Observations of clouds, aerosols, precipitation, and surface radiation over the Southern Ocean: an overview of CAPRICORN, MARCUS, MICRE, and SOCRATES. *Bull. Am. Meteorol. Soc.* **102**, E894–E928 (2021).
- Mallet, M. D., Alexander, S. P., Protat, A. & Fiddes, S. L. Reducing Southern Ocean shortwave radiation errors in the ERA5 reanalysis with machine learning and 25 years of surface observations. *Artif. Intell. Earth Syst.* **2**, e220044 (2023).
- Wood, R. Stratus and stratocumulus. *Encycl. Atmos. Sci.* **2**, 196–200 (2015).
- Chen, T., Rossow, W. B. & Zhang, Y. Radiative effects of cloud-type variations. *J. Clim.* **13**, 264–286 (2000).
- Lodise, J. et al. Global climatology of extratropical cyclones from a new tracking approach and associated wave heights from satellite radar altimeter. *J. Geophys. Res.: Oceans* **127**, e2022JC018925 (2022).
- Fernández-Barba, M., Belyaev, O., Huertas, I. E. & Navarro, G. Marine heatwaves in a shifting Southern Ocean induce dynamical changes in primary production. *Commun. Earth Environ.* **5**, 404 (2024).
- Armour, K. C., Marshall, J., Scott, J. R., Donohoe, A. & Newsom, E. R. Southern Ocean warming delayed by circumpolar upwelling and equatorward transport. *Nat. Geosci.* **9**, 549–554 (2016).
- Hu, Y., Tian, W., Dong, Y. & Zhang, J. Evaluating the seasonal responses of Southern Ocean sea surface temperature to Southern Annular Mode in CMIP6 models. *Geophys. Res. Lett.* **51**, e2024GL108782 (2024).
- Dong, S., Gille, S. T. & Sprintall, J. An assessment of the Southern Ocean mixed layer heat budget. *J. Clim.* **20**, 4425–4442 (2007).
- Simmonds, I. Modes of atmospheric variability over the Southern Ocean. *J. Geophys. Res.: Oceans* **108**, SOV5 (2003).
- Josey, S. A., Grist, J. P., Mecking, J. V., Moat, B. I. & Schulz, E. A clearer view of Southern Ocean air–sea interaction using surface heat flux asymmetry. *Philos. Trans. R. Soc. A* **381**, 20220067 (2023).
- Nakamura, H., Sampe, T., Tanimoto, Y. & Shimpo, A. In *Geophysical Monograph Series* (eds Wang, C. et al.) 329–345 (American Geophysical Union, 2004).
- Nakamura, H., Sampe, T., Goto, A., Ohfuchi, W. & Xie, S. On the importance of midlatitude oceanic frontal zones for the mean state and dominant variability in the tropospheric circulation. *Geophys. Res. Lett.* **35**, 2008GL034010 (2008).
- Sampe, T., Nakamura, H., Goto, A. & Ohfuchi, W. Significance of a midlatitude SST frontal zone in the formation of a storm track and an eddy-driven westerly jet. *J. Clim.* **23**, 1793–1814 (2010).
- Ogawa, F., Nakamura, H., Nishii, K., Miyasaka, T. & Kuwano-Yoshida, A. Importance of midlatitude oceanic frontal zones for the annular mode variability: interbasin differences in the Southern Annular Mode signature. *J. Clim.* **29**, 6179–6199 (2016).
- Sallée, J. B., Speer, K. G. & Rintoul, S. R. Zonally asymmetric response of the Southern Ocean mixed-layer depth to the Southern Annular Mode. *Nat. Geosci.* **3**, 273–279 (2010).
- Lin, X., Zhai, X., Wang, Z. & Munday, D. R. Mean, variability, and trend of Southern Ocean wind stress: role of wind fluctuations. *J. Clim.* **31**, 3557–3573 (2018).
- Pednekar, S. M. Trends and interannual variability of satellite-based wind and sea surface temperature over the Southern Ocean in the recent decade. *Int. J. Geosci.* **6**, 145–158 (2015).
- Styles, A. F., MacGilchrist, G. A., Bell, M. J. & Marshall, D. P. Spatial and temporal patterns of Southern Ocean ventilation. *Geophys. Res. Lett.* **51**, e2023GL106716 (2024).
- Doddridge, E. W. & Marshall, J. Modulation of the seasonal cycle of Antarctic sea ice extent related to the Southern Annular Mode. *Geophys. Res. Lett.* **44**, 9761–9768 (2017).

43. Marshall, J. & Speer, K. Closure of the meridional overturning circulation through Southern Ocean upwelling. *Nat. Geosci.* **5**, 171–180 (2012).
44. Prend, C. J. et al. Indo-Pacific sector dominates Southern Ocean carbon outgassing. *Glob. Biogeochem. Cycles* **36**, e2021GB007226 (2022).
45. du Plessis, M., Swart, S., Ansorge, I. J. & Mahadevan, A. Submeso-scale processes promote seasonal restratification in the subantarctic ocean. *J. Geophys. Res.: Oceans* **122**, 2960–2975 (2017).
46. Viglione, G. A., Thompson, A. F., Flexas, M. M., Sprintall, J. & Swart, S. Abrupt transitions in submesoscale structure in southern Drake Passage: glider observations and model results. *J. Phys. Oceanogr.* **48**, 2011–2027 (2018).
47. Prend, C. J. et al. Observing system requirements for measuring high-frequency air–sea fluxes in the Southern Ocean. *Elem. Sci. Anth.* **13**, 00061 (2025).
48. Priestley, M. D. K. et al. An overview of the extratropical storm tracks in CMIP6 historical simulations. *J. Clim.* **33**, 6315–6343 (2020).
49. Bodas-Salcedo, A. et al. Origins of the solar radiation biases over the Southern Ocean in CFMIP2 models. *J. Clim.* **27**, 41–56 (2014).
50. Ogle, S. E. et al. Episodic Southern Ocean heat loss and its mixed layer impacts revealed by the farthest south multiyear surface flux mooring. *Geophys. Res. Lett.* **45**, 5002–5010 (2018).
51. Tamsitt, V., Cerovečki, I., Josey, S. A., Gille, S. T. & Schulz, E. Mooring observations of air–sea heat fluxes in two subantarctic mode water formation regions. *J. Clim.* **33**, 2757–2777 (2020).
52. Jones, J. M. et al. Assessing recent trends in high-latitude Southern Hemisphere surface climate. *Nat. Clim. Change* **6**, 917–926 (2016).
53. Fogt, R. L. & Marshall, G. J. The Southern Annular Mode: variability, trends, and climate impacts across the Southern Hemisphere. *WIREs Clim. Change* **11**, e652 (2020).
54. Reboita, M. S., Da Rocha, R. P., Ambrizzi, T. & Gouveia, C. D. Trend and teleconnection patterns in the climatology of extratropical cyclones over the Southern Hemisphere. *Clim. Dyn.* **45**, 1929–1944 (2015).
55. Reynolds, R. W., Rayner, N. A., Smith, T. M., Stokes, D. C. & Wang, W. An improved in situ and satellite SST analysis for climate. *J. Clim.* **15**, 1609–1625 (2002).

**Publisher's note** Springer Nature remains neutral with regard to jurisdictional claims in published maps and institutional affiliations.

**Open Access** This article is licensed under a Creative Commons Attribution 4.0 International License, which permits use, sharing, adaptation, distribution and reproduction in any medium or format, as long as you give appropriate credit to the original author(s) and the source, provide a link to the Creative Commons licence, and indicate if changes were made. The images or other third party material in this article are included in the article's Creative Commons licence, unless indicated otherwise in a credit line to the material. If material is not included in the article's Creative Commons licence and your intended use is not permitted by statutory regulation or exceeds the permitted use, you will need to obtain permission directly from the copyright holder. To view a copy of this licence, visit <http://creativecommons.org/licenses/by/4.0/>.

© The Author(s) 2025

## Methods

### Observational campaign

The observations in this study were made as a part of the SOSCEX-Storm experiment, aiming to simultaneously observe how storms impact the upper ocean in the subpolar Southern Ocean and the response to air–sea heat and CO<sub>2</sub> exchange<sup>56</sup>. The SOSCEX-Storm experiment fits into the larger observational programme of the Southern Ocean Seasonal Cycle Experiment<sup>57</sup>. SOSCEX-Storm undertook a twinned deployment of an autonomous surface vehicle, Wave Glider and a profiling buoyancy Slocum glider (Extended Data Fig. 1b–e). The two vehicles were piloted in conjunction with each other (Extended Data Fig. 1b), allowing for a coupled high-resolution view of the atmosphere and upper-ocean response. The field site was located at 54° S, 0° E, south of the Polar Front where the ocean was subjected to among the highest air–sea heat fluxes and wind speeds of the Southern Ocean (Extended Data Fig. 1a). The platforms were deployed and retrieved from the R/V S.A. Agulhas II and sampled together between 20 December 2018 and 8 March 2019 (79 days).

**Slocum glider with RSI MicroRider.** The Webb Teledyne G2 Slocum glider housed a Rockland Scientific Microstructure Profiler (MicroRider) that was piloted in a north–south fence mode of length 14 km to reveal the impact of storms on the turbulent mixing of the upper ocean (Extended Data Fig. 1b,e). The MicroRider was equipped with two piezo-electric accelerometers and two air-foil shear probes oriented orthogonally. Microstructure data were only collected during the glider climbs to prolong battery life and obtain dissipation estimates as close to the surface as possible. The glider was equipped with a continuously pumped Seabird Slocum Glider conductivity, temperature and depth (CTD) sensor, which was processed with the GEOMAR MATLAB toolbox and vertically gridded into 1-m bins using a linear interpolation. Initial data processing removed temperature data from the upper 2 m during the glider climb phase, and so to obtain an SST value from the Slocum glider temperature profiles, we calculated the median value between 0.5-m and 10-m depth for each dive. By taking the median value, we ensure any spurious data are neglected in the surface ocean boundary layer. Nicholson et al.<sup>56</sup> provide details on the MicroRider processing. Using the glider CTD temperature profiles, we calculate the MLD as the depth from where the temperature first exceeds the 10-m reference value by 0.2 °C, following de Boyer Montegut et al.<sup>58</sup>.

**Liquid Robotics Wave Glider.** The Liquid Robotics SV3 Wave Glider was fitted with an Airmar WX-200 Ultrasonic Weather Station mounted on a mast at 0.7 m above sea level (Extended Data Fig. 1d), providing wind-speed measurements at a rate of 1 Hz, averaged into 1-hour bins. The wind measurements were corrected to a height of 10-m above sea level<sup>59</sup>. The Wave Glider stopped collecting wind measurements on 12 February 2019, and so the remainder of the wind-speed time series was completed with co-located ERA5 wind speed, which showed a strong correlation ( $r^2 = 0.8$ ) with the in situ wind-speed observations. The Wave Glider was piloted in a figure-of-8 pattern directly above the Slocum glider, providing continuous co-located measurements of the lower atmosphere wind speed and upper-ocean variability (Extended Data Fig. 1b).

### Datasets

**ERA5 reanalysis.** In this study, we use the fifth-generation European Centre for Medium Range Weather Forecasts reanalysis for the global climate and weather (ERA5) wind speed, calculated from the output of the  $u$ - and  $v$ -component of the wind at 10-m above the surface of Earth, and the four components of the air–sea heat flux, namely the sensible, latent, net surface solar radiation and net surface thermal radiation. ERA5 reanalysis combines model data with observations from across the world into a globally complete dataset. The net radiation components referred to above are determined by subtracting the

downwelling from the upwelling components. The sign convention is downward positive, where ocean heat gain is due to a positive heat flux. ERA5 global atmospheric reanalysis was provided on a  $0.25^\circ \times 0.25^\circ$  horizontal grid and at hourly time intervals and is fundamental for this study as it provides an important source of data to determine storm locations (storm classification method below) and crucially, determine the impacts of storms-associated wind speed and air–sea heat flux on the interannual SST variability. We used the ERA5 product instead of other commonly used reanalyses, such as Japanese 55-year Reanalysis (JRA-55) and National Centers for Environmental Prediction (NCEP), as it has been shown to produce robust correlations to the high Southern Ocean wind speeds<sup>59</sup> and heat fluxes<sup>51,60,61</sup> across synoptic timescales. All reanalysis data within sea ice have not been used in this analysis.

**Satellite sea surface temperature.** Monthly SST data were obtained from the National Oceanic and Atmospheric Administration (NOAA) optimum interpolation (OI) SST V2 product, which uses both in situ and satellite data from November 1981 to January 2023<sup>55</sup>. Data are provided by the National Centers for Environmental Prediction and made available on a  $1^\circ$  grid. All SST data where co-located sea-ice concentrations—obtained from the NOAA OI SST V2 product<sup>55</sup>—were above 0 have been removed from this analysis.  $T_{\max}$  is obtained by finding the maximum SST for each summer period.

**EN4.** We use the version 4 of the Met Office Hadley Centre “EN” series of data sets of global quality controlled ocean temperature and salinity profiles (EN4) from 2004 to 2019 to produce our MLD for the interannual analysis<sup>62,63</sup>. We use the profiles that contain the Cheng et al.<sup>64</sup> Expendable Bathythermograph (XBT) corrections and Gouretski and Cheng<sup>65</sup> Mechanical Bathythermograph (MBT) corrections. We limit the data intake to 2004 as this marks the beginning of the Argo period. To calculate the MLD from the EN4 data, we use the  $0.03 \text{ kg m}^{-3}$  density threshold of de Boyer Montegut et al.<sup>58</sup>. To obtain the MLD for each summer season, we first calculate the MLD for each individual profile and then find the median MLD value for each month within  $2^\circ \times 2^\circ$  grid cells. This provides good coverage of summer MLD values across the Southern Ocean, which is valuable for limiting spatial bias (Extended Data Fig. 9).

Whereas the MLD demonstrates broad-scale agreement in its interannual variability with the wind speed and  $T_{\max}$  (Fig. 5b), it is important to acknowledge that MLD estimates are limited to low spatio-temporal resolution datasets. Consequently, the influence of smaller-scale ocean dynamics, which can substantially affect the MLD, may not be fully captured<sup>45,46,66</sup>. For instance, submesoscale eddies are known to restratify the ocean and thus would be expected to counteract storm-driven mixing in regions of high eddy energy, potentially contributing to a higher  $T_{\max}$ <sup>67</sup>. These submesoscale dynamics are probably most prevalent in eddy-rich regions, such as along the Antarctic Circumpolar Current<sup>45</sup>, which may account for the statistically insignificant correlations there.

**Southern Annular Mode.** The SAM is the principal mode of variability in the atmospheric circulation of the Southern Hemisphere mid and high latitudes<sup>68</sup>. We use the Marshall SAM Index, obtained from station-based observations of the zonal pressure difference between the latitudes of 40° S and 65° S. A positive index value indicates a positive SAM phase, and a negative value indicates a negative phase.

### Storm classification

We obtain storm locations from Lodise et al.<sup>27</sup>, who determine the central position of all Southern Hemisphere mid-latitude cyclones between 1981 to 2019. Specifically, they use a Lagrangian tracking algorithm on the ERA5 mean sea-level pressure (MSLP) fields that finds MSLP minima co-located with the Laplacian of the MSLP,  $\nabla^2 p = \left( \frac{\partial^2 p}{\partial x^2} + \frac{\partial^2 p}{\partial y^2} \right)$ . We define the storm area as a 1,000-km radius

extending from the central pressure of each mid-latitude cyclone. We only include storms that have a central location south of 40° S and remove all storms within 500 km of land. We only use storms occurring in the months of December to February, totalling 578,721 hourly storm occurrences between 1981 and 2019.

### Mixed-layer tendency budget

To investigate the contributions of air–sea heat fluxes and vertical entrainment to the tendency of SST, we used a simplified mixed-layer temperature budget:

$$\frac{T_m}{\partial t} = \frac{Q_{\text{net}} - Q_{\text{pen}}}{\rho_0 C_p h_m} - \frac{w_e \Delta T_m}{h_m} \quad (1)$$

In equation (1), the left-hand side corresponds to the tendency terms for temperature ( $^{\circ}\text{C s}^{-1}$ ), while  $Q_{\text{net}}$  is the net surface heat flux ( $\text{W m}^{-2}$ ) and  $Q_{\text{pen}}$  is the flux penetrating the base of the mixed layer ( $\text{W m}^{-2}$ ),  $\rho_0$  a reference density ( $1,025 \text{ kg m}^{-3}$ ),  $C_p$  the specific heat capacity of seawater ( $3,850 \text{ J kg}^{-1} \text{ K}^{-1}$ ) and  $h_m$  is the mixed-layer depth.  $w_e$  is the entrainment velocity ( $\text{m s}^{-1}$ ) taken as  $\partial h_m / \partial t$ , while  $\Delta T_m$  corresponds to the temperature difference between the base of the mixed layer and 5 m below the MLD.

Entrainment was considered here as an irreversible flux of temperature into the mixed layer from below as a result of a deepening mixed layer. The rate that entrainment takes place was given by

$$w_e = \mathcal{H} \left( \frac{\partial h_m}{\partial t} \right) \quad (2)$$

Using  $x = \text{MLD}(t) / \text{MLD}(t-1)$ ,

$$\mathcal{H}(x) = \begin{cases} 1, & \text{if } x \geq 1 \\ 0, & \text{if } x \leq 1. \end{cases} \quad (3)$$

### Summertime SST change due to Ekman transport

The integrated heat flux in the Ekman layer due to Ekman advection<sup>38</sup> was determined following:

$$Q_{\text{EK}} = \rho C_p (U_E \cdot \nabla \text{SST}) \quad (4)$$

$U_E$  is the total Ekman transport, defined as:

$$U_E = \frac{1}{\rho f} (\tau_y, -\tau_x) \quad (5)$$

where  $\rho$  is the density of seawater, taken as  $1,027 \text{ kg m}^{-3}$ .  $f$  is the Coriolis parameter.  $\tau_y$ ,  $\tau_x$  are the meridional and zonal wind stress components. The SST gradient,  $\nabla \text{SST}$ , is the gradient with respect to longitude ( $x$ ) and latitude ( $y$ ):

$$\nabla \text{SST} = \left( \frac{\partial \text{SST}}{\partial x}, \frac{\partial \text{SST}}{\partial y} \right) \quad (6)$$

The vertically integrated Ekman heat transport is distributed over the Ekman layer depth ( $D_e$ )<sup>69,70</sup>, with its impact on the mixed-layer temperature (or equivalently the SST) tendency is given by:

$$\frac{\partial T}{\partial t} = \frac{Q_{\text{EK}}}{\rho C_p D_e} \quad (7)$$

The Ekman layer depth,  $D_e$ , is determined by:  $D_e = \sqrt{2A/f}$ , where  $A$  is the eddy viscosity following  $A = \kappa u_* z$ , with  $\kappa$  representing the von Karman constant (0.4),  $u_*$  the friction velocity ( $u_* = \sqrt{\tau/\rho}$ ) and  $z$  the depth at which eddy viscosity is being assumed, taken as 10 m.

We determine  $\partial T / \partial t$  at daily timescales and then integrate over each summer period between 1981 to 2019 to approximate the total SST change associated with Ekman transport for each season.

### Data availability

All quality-controlled data that support the findings of this study are available via Zenodo at <https://doi.org/10.5281/zenodo.13075265> (ref. 71), including the storm tracks. EN4 data used to determine the MLD are available at <https://www.metoffice.gov.uk/hadobs/en4/>. NOAA OI SST and sea ice are available at <https://psl.noaa.gov/data/gridded/data.noaa.oisst.v2.html>. ERA5 reanalysis data are available at <https://doi.org/10.24381/cds.bd0915c6>. SAM Index data are available at <https://climatedataguide.ucar.edu/climate-data/marshall-southern-annular-mode-sam-index-station-based>. MODIS L2 cloud top pressure data are available at [https://ladsweb.modaps.eosdis.nasa.gov/missions-and-measurements/products/MYD06\\_L2](https://ladsweb.modaps.eosdis.nasa.gov/missions-and-measurements/products/MYD06_L2).

### Code availability

The computer code used for data processing and analysis is available via Github at <https://github.com/marcelduplessis/duplessis-storms-warming>.

### References

- Nicholson, S.-A. et al. Storms drive outgassing of CO<sub>2</sub> in the subtropical Southern Ocean. *Nat. Commun.* **13**, 158 (2022).
- Swart, S. et al. Southern Ocean seasonal cycle experiment 2012: seasonal scale climate and carbon cycle links. *South Afr. J. Sci.* **108**, 11–13 (2012).
- de Boyer Montégut, C., Madec, G., Fischer, A. S., Lazar, A. & Iudicone, D. Mixed layer depth over the global ocean: an examination of profile data and a profile-based climatology. *J. Geophys. Res.: Oceans* **109**, 2004JC002378 (2004).
- Schmidt, K. M., Swart, S., Reason, C. & Nicholson, S.-A. Evaluation of satellite and reanalysis wind products with in situ wave glider wind observations in the Southern Ocean. *J. Atmos. Oceanic Technol.* **34**, 2551–2568 (2017).
- Swart, S. et al. Constraining southern ocean air-sea-ice fluxes through enhanced observations. *Front. Mar. Sci.* **6**, 421 (2019).
- du Plessis, M. D. et al. The daily-resolved Southern Ocean mixed layer: regional contrasts assessed using glider observations. *J. Geophys. Res.: Oceans* **127**, e2021JC017760 (2022).
- Roemmich, D. & Gilson, J. The 2004–2008 mean and annual cycle of temperature, salinity, and steric height in the global ocean from the Argo Program. *Prog. Oceanogr.* **82**, 81–100 (2009).
- Good, S. A., Martin, M. J. & Rayner, N. A. EN4: quality controlled ocean temperature and salinity profiles and monthly objective analyses with uncertainty estimates: the EN4 data set. *J. Geophys. Res.: Oceans* **118**, 6704–6716 (2013).
- Cheng, L., Zhu, J., Cowley, R., Boyer, T. & Wijffels, S. Time, probe type, and temperature variable bias corrections to historical expendable bathythermograph observations. *J. Atmos. Oceanic Technol.* **31**, 1793–1825 (2014).
- Gouretski, V. & Cheng, L. Correction for systematic errors in the global dataset of temperature profiles from mechanical bathythermographs. *J. Atmos. Oceanic Technol.* **37**, 841–855 (2020).
- du Plessis, M., Swart, S., Anson, I. J., Mahadevan, A. & Thompson, A. F. Southern Ocean seasonal restratification delayed by submesoscale wind-front interactions. *J. Phys. Oceanogr.* **49**, 1035–1053 (2019).
- Su, Z., Wang, J., Klein, P., Thompson, A. F. & Menemenlis, D. Ocean submesoscales as a key component of the global heat budget. *Nat. Commun.* **9**, 775 (2018).
- Marshall, G. J. Trends in the Southern Annular Mode from observations and reanalyses. *J. Clim.* **16**, 4134–4143 (2003).

69. Madsen, O. S. A realistic model of the wind-induced Ekman boundary layer. *J. Phys. Oceanogr.* **7**, 248–255 (1977).
70. Weller, R. A. & Plueddemann, A. J. Observations of the vertical structure of the oceanic boundary layer. *J. Geophys. Res.: Oceans* **101**, 8789–8806 (1996).
71. du Plessis, M. et al. Data used in 'Southern Ocean summer warming is regulated by storm-driven mixing'. *Zenodo* <https://doi.org/10.5281/zenodo.13075265> (2024).

## Acknowledgements

We are grateful to all scientists and support staff who helped in data collection, in particular Sea Technology Services for technical assistance with glider deployments and the South African National Antarctic Program (SANAP), the captain and crew of the S. A. Agulhas II for their fieldwork/technical assistance. We thank G. Krahnemann at GEOMAR (Research Center for Marine Geosciences) for assistance with software tools for processing Slocum data and I. Fer for the help with processing of the Microstructure data. M.D.d.P., S.-A.N., S.S. and P.M.S.M. were supported by the European Union's Horizon 2020 research and innovation programme under grant agreement number 821001 (SO-CHIC). M.D.d.P. was also supported by the European Union's Marie Skłodowska Curie Individual Fellowship under Project ID 101032683 and Swedish Research Council Grant (VR 2024-05841). S.S. was supported by a Wallenberg Academy Fellowship (WAF 2015.0186) and the Swedish Research Council (Vetenskapsrådet; VR 2019-04400) grant. S.S. and M.D.d.P. have received funding from the European Research Council's (ERC) Horizon Europe Synergy Grant programme under grant agreement number 101118693 (WHIRLS). I.G. was supported by the VR-International Postdoctoral Grant (number 253001101). S.-A.N. was supported by South African National Antarctic Program Grant under grant agreement number SANAP230503101416. C.J.P. was supported by a NOAA Climate

and Global Change Postdoctoral Fellowship and a Fulbright US Scholar Award.

## Author contributions

M.D.d.P. conceived the study, performed the analysis and wrote the paper. S.-A.N. conceived the experimental idea and approach and contributed to interpretation of the analysis. S.S. was involved in carrying out the experimental design and contributed to the interpretation of the analysis. I.G. and C.J.P. contributed to the interpretation of the analysis. P.M.S.M. conceived the experimental idea and approach. All authors contributed to revising the draft paper.

## Funding

Open access funding provided by University of Gothenburg.

## Competing interests

The authors declare no competing interests.

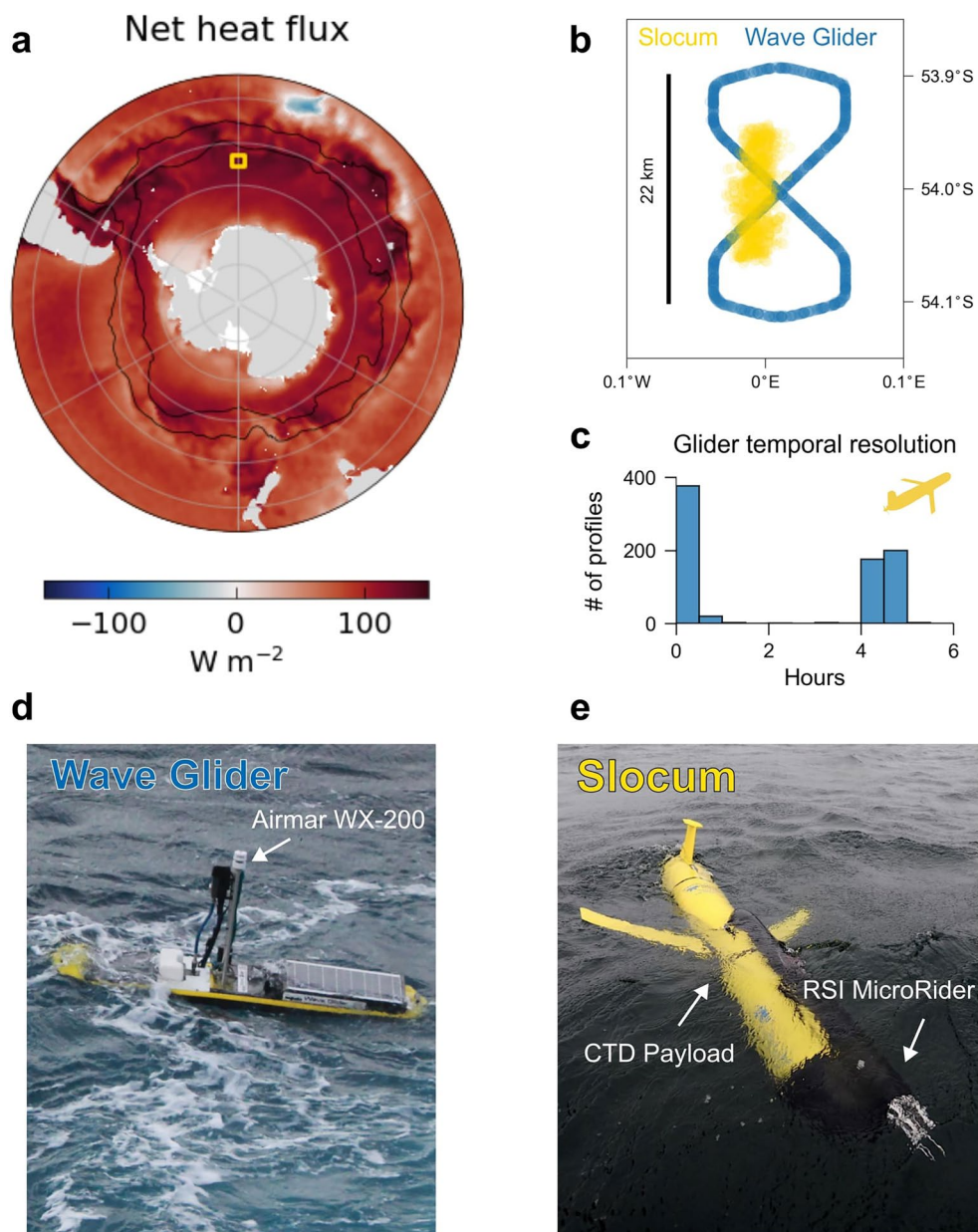
## Additional information

**Extended data** is available for this paper at <https://doi.org/10.1038/s41561-025-01857-3>.

**Correspondence and requests for materials** should be addressed to Marcel D. du Plessis.

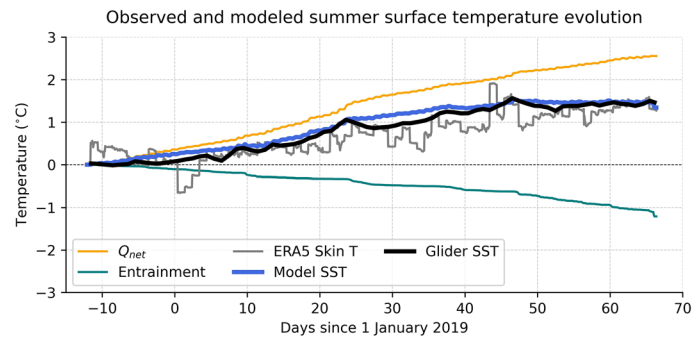
**Peer review information** *Nature Geoscience* thanks Earle Wilson and the other, anonymous, reviewer(s) for their contribution to the peer review of this work. Primary Handling Editors: Aliénor Lavergne, Tom Richardson and James Super, in collaboration with the *Nature Geoscience* team.

**Reprints and permissions information** is available at [www.nature.com/reprints](http://www.nature.com/reprints).



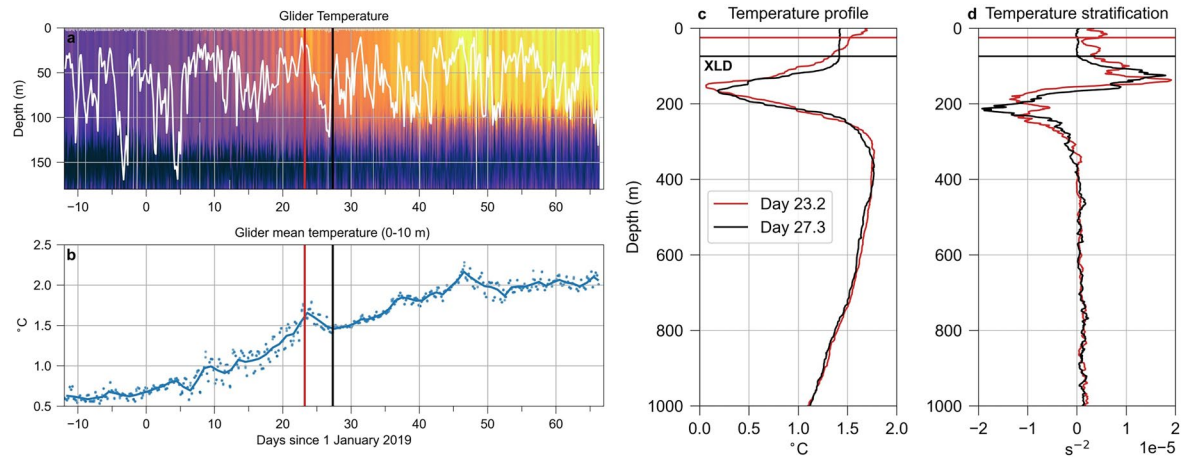
**Extended Data Fig. 1 | SOSCEX-Storm field campaign and robotic platforms.** **a**, The mean net air-sea heat flux for the period of SOSCEX-Storm (December 2018 to February 2019) using ERA5 reanalysis. The location of the robotic field deployments is shown as the yellow box. **b**, Tracks of the underwater Slocum glider (yellow) and surface Wave Glider (blue). **c**, Histogram of the time between

underwater Slocum glider surfacing, indicating the temporal resolution of the sea surface temperature. Images of the **d**, surface Wave Glider and **e**, underwater Slocum glider used during the SOSCEX-Storm field campaign. Basemap in **a** from Natural Earth (<https://www.naturalearthdata.com>). Photographs courtesy of Dr. Sarah Nicholson.



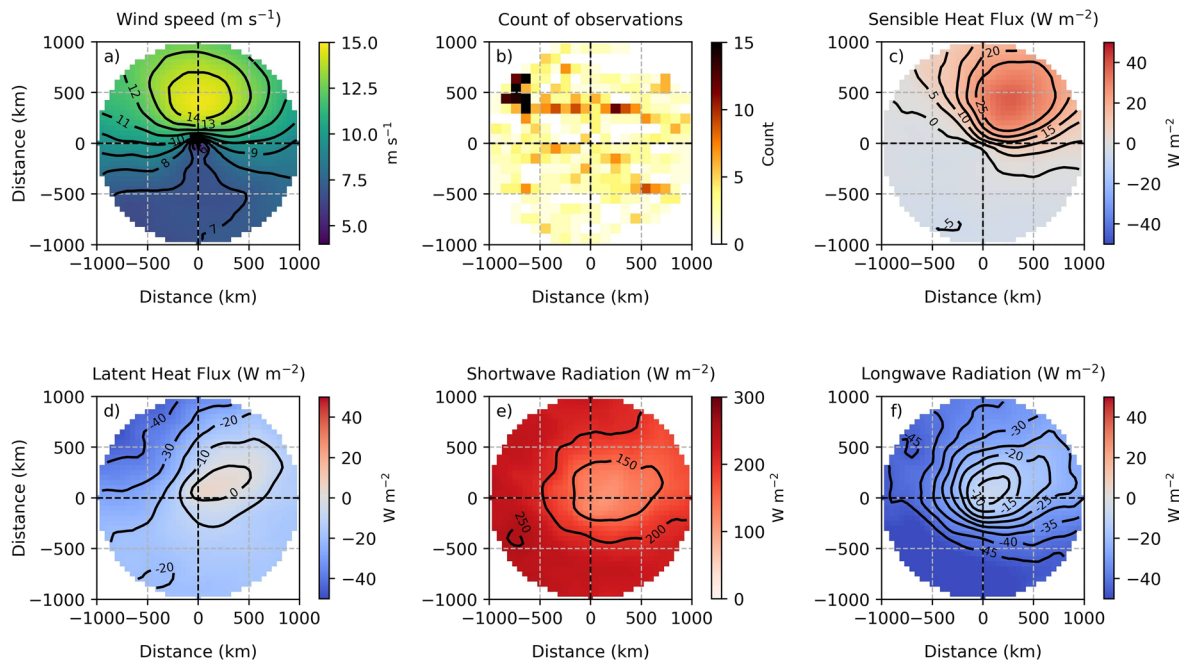
**Extended Data Fig. 2 | Modeled contributions to observed summer sea surface temperature evolution.** The daily evolution of sea surface temperature (SST) is shown relative to its value on deployment of the robotic platforms. The modeled SST (blue line) represents the net temperature change derived from cumulative

net heat flux ( $Q_{net}$ , orange line) and entrainment (teal line). These are compared with independent glider SST observations (black line) and co located ERA5 skin temperature (grey line).



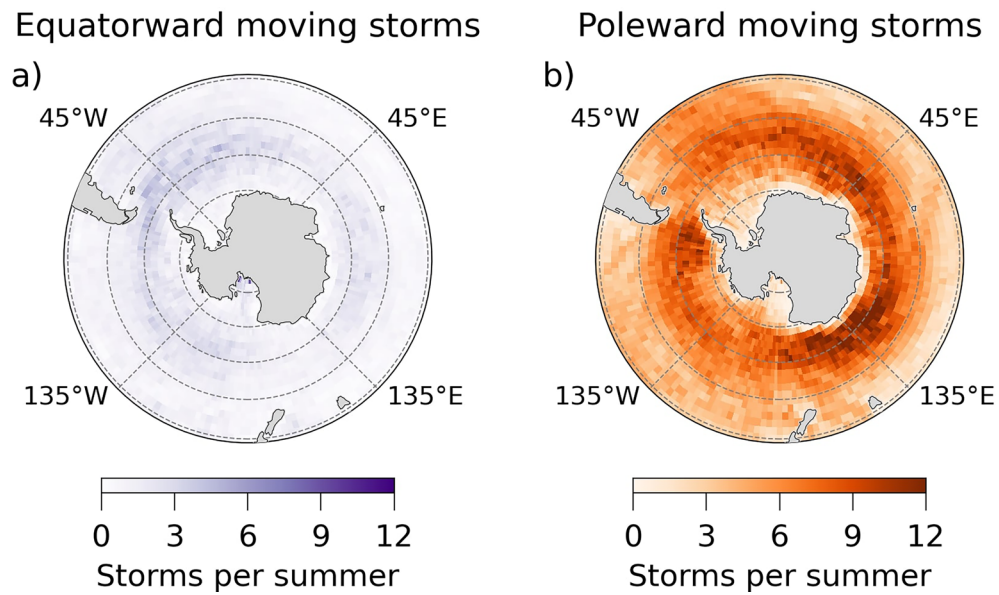
**Extended Data Fig. 3 | Storm-driven entrainment drives strong SST cooling.**  
**a.**, Summer evolution of the upper ocean temperature (color, °C) from the underwater glider, with the mixing layer depth (XLD, white line) defined from the MicroRider measurements on the Slocum. The red and black lines show the times of the two profiles compared in **c** and **d**. **b**, Time series of the sea surface

temperature (SST) from the underwater glider observations (line shows the daily-mean). Vertical profiles of **c**, temperature, and **d**, thermal component of the Brunt-Väisälä frequency from the underwater glider before (red, day 23.2) and after (black, day 27.3) the storm encountered on 24 January 2019. The respective horizontal lines depict the depth of the XLD for each given profile.

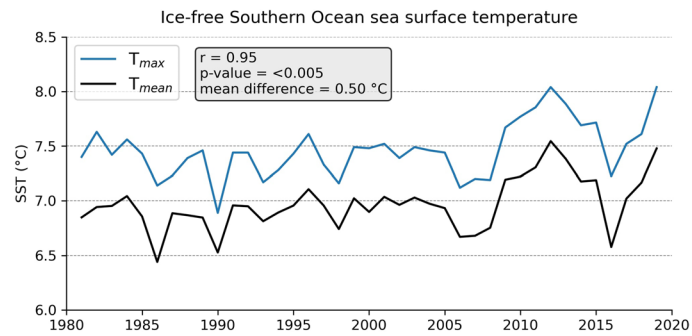


**Extended Data Fig. 4 | Summer-mean ERA5 wind speed and air-sea heat flux components within storms overlapping with the SOSCEX-Storm field campaign. a**, Mean wind speed ( $\text{m s}^{-1}$ ) for all storms during SOSCEX-Storm within 1000 km of the robotic observations, and **b**, count of underwater glider

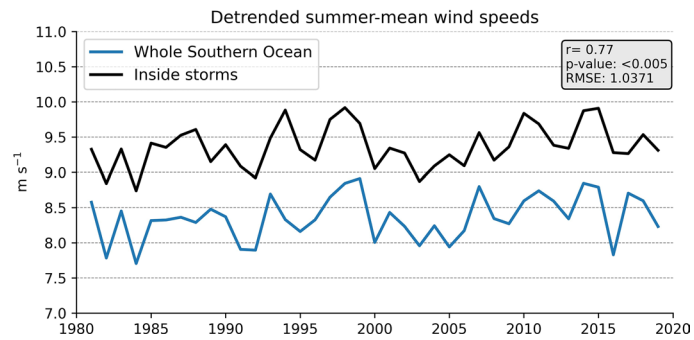
observations relative to the storm position. **c-f**, mean of the sensible heat flux, latent heat flux, shortwave radiation, and longwave radiation for all storms in  $\text{W m}^{-2}$ , respectively. Contour lines represent the mean wind speed in **a**, and the respective mean heat flux values in **c** through **f**.



**Extended Data Fig. 5 | Distribution maps of equatorward and poleward Southern Ocean storm trajectories between 1981 and 2019.** **a**, Average number of equatorward-moving storms per summer. **b**, Average number of poleward-moving storms per summer. Storm track positions were obtained from ref.2. Basemaps from Natural Earth (<https://www.naturalearthdata.com>).

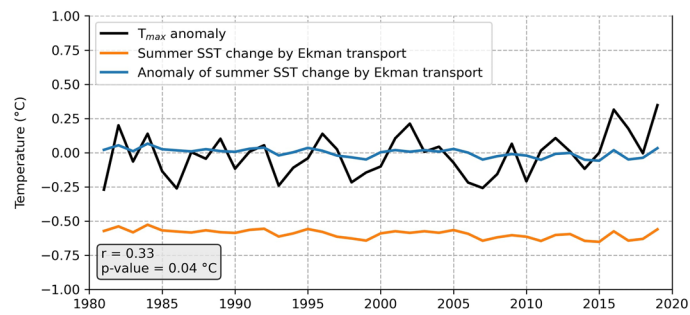


**Extended Data Fig. 6 | Ice-free Southern Ocean summer maximum and mean sea surface temperature variability.** Time series of the median value of the ice-free Southern Ocean summer maximum ( $T_{max}$ , blue) and summer mean ( $T_{mean}$ , black) sea surface temperature from 1981 to 2019. The correlation ( $r=0.95$ ) between  $T_{max}$  and  $T_{mean}$  indicates a strong significant ( $p < 0.005$ ,  $n=39$ ) coherence between the two.

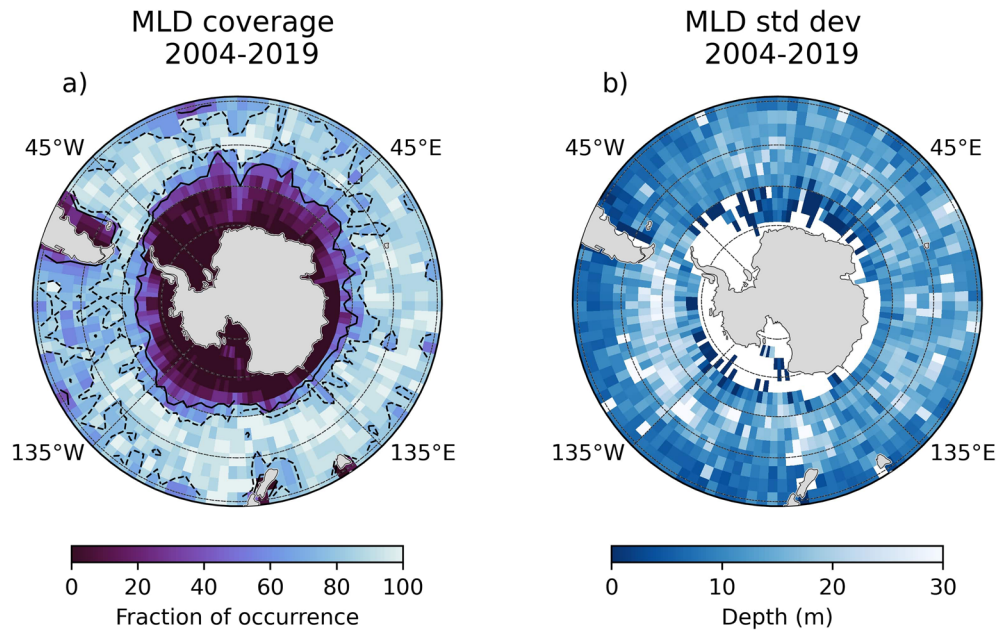


**Extended Data Fig. 7 | Summer-mean of the detrended wind speed inside storms vs. the whole ice-free Southern Ocean.** Interannual variability of the summer-mean detrended wind speed ( $\text{m s}^{-1}$ ) inside storms (black line) and

over the whole ice-free Southern Ocean (blue line) for the period 1981 to 2019. Both time series show strong significant ( $p < 0.005$ ,  $n=39$ ) coherence, with a correlation coefficient of  $r=0.77$ .



**Extended Data Fig. 8 | Comparison between summer SST anomalies and Ekman-driven temperature changes from 1981 to 2019.** Time series of the Southern Ocean summer maximum sea surface temperature anomaly ( $T_{max}$ , black line), and the Southern Ocean-mean Ekman-driven summer SST change (orange line, anomaly shown as the blue line). All quantities are expressed in °C.



**Extended Data Fig. 9 | Coverage and standard deviation of the Southern Ocean mixed layer depth between 2004 and 2019.** **a**, The fraction occurrence (in percent) that a summer-mean mixed layer depth (MLD) was observed within the 16 years. Black contours indicate 50% (solid line) and 80% (dashed line) MLD

coverage. **b**, Standard deviation of the summer-mean MLD over the 16 years, indicating the variability in MLD. Basemaps from Natural Earth (<https://www.naturalearthdata.com>).